.

# Three-dimensional ring current decay model

Mei-Ching Fok and Thomas E. Moore

Space Sciences Laboratory, NASA Marshall Space Flight Center, Huntsville, Alabama

Janet U. Kozyra

Space Physics Research Laboratory, Department of Atmospheric, Oceanic and Space Sciences, University of
Michigan, Ann Arbor

George C. Ho and Douglas C. Hamilton

Department of Physics, University of Maryland, College Park

**Abstract.** This work is an extension of a previous ring current decay model. In the previous
work, a two-dimensional kinetic model was constructed to study the temporal variations of the
equatorially mirroring ring current ions, considering charge exchange and Coulomb drag losses
along drift paths in a magnetic dipole field. In this work, particles with arbitrary pitch angle are
considered. By bounce averaging the kinetic equation of the phase space density, information
along magnetic field lines can be inferred from the equator. The three-dimensional model is used
to simulate the recovery phase of a model great magnetic storm, similar to that which occurred
in early February 1986. The initial distribution of ring current ions (at the minimum $Dst$) is
extrapolated to all local times from AMPTE/CCE spacecraft observations on the dawnside and
duskside of the inner magnetosphere spanning the $L$ value range $L = 2.25$ to $6.75$. Observations
by AMPTE/CCE of ring current distributions over subsequent orbits during the storm recovery
phase are compared to model outputs. In general, the calculated ion fluxes are consistent with
observations, except for $H^+$ fluxes at tens of keV, which are always overestimated. A newly
invented visualization idea, designated as a chromogram, is used to display the spatial and energy
dependence of the ring current ion differential flux. Important features of storm time ring current,
such as day-night asymmetry during injection and drift hole on the dayside at low energies (<10
keV), are manifested in the chromogram representation. The pitch angle distribution is well fit
by the function, $j_0(1 + Ay^n)$, where $y$ is sine of the equatorial pitch angle. The evolution of the
index $n$ is a combined effect of charge exchange loss and particle drift. At low energies (<30
keV), both drift dispersion and charge exchange are important in determining $n$.

## 1. Introduction

A two-dimensional kinetic model was previously developed
to study the ring current dynamics during the recovery phase of
magnetic storm and the associated aeronomical effects, con-
sidering only equatorially mirroring particles. The model
solved for the temporal variations of the phase space densities
of each ring current ion species, considering charge exchange
and Coulomb drag losses along drift paths. The details of the
model and its first results, obtained by simulating a moderate
storm, were presented by *Fok et al.* [1993] (hereafter referred
to as paper 1). The model successfully reproduced some ob-
servable features in the storm time ring current distribution
functions and the calculated plasmaspheric heating was found
to be sufficient to power the subauroral $T_e$ peak and the stable
auroral red (SAR) arc emissions at levels consistent with ob-
servations. A new finding of the model was that it predicted
the formation of a low-energy (<500 eV) ion population, as a
result of energy degradation of ring current ions through
Coulomb collisions with the plasmasphere.

Although quite a few ring current models have been devel-
oped [*Harel et al.*, 1981; *Kistler et al.*, 1989; *Sheldon*, 1994;
*Chen et al.*, 1994], most of them are either restricted to equato-
rially mirroring particles or assume isotropic pitch angle dis-
tribution. In this work, ring current ions of all pitch angles are
considered. This spatially three-dimensional problem is re-
duced to two dimensions by bounce averaging the kinetic equa-
tion of phase space density. This approach is valid since the
bounce periods of ring current ions (1 < E < 300 keV) are much
shorter than the charge exchange and Coulomb decay lifetimes
[*Rycroft*, 1987]. That is, ring current ions experience in-
significant loss within a bounce. Thus the ion differential flux
can be assumed to be constant along the field line between
mirror points. A model major magnetic storm which is similar
to the great storm in February 1986 is simulated to examine
the temporal evolution of the ring current population and
pitch angle distribution during a major storm. The initial (at
the minimum $Dst$) distributions of three major ring current ion
species ($H^+$, $He^+$, and $O^+$) are extrapolated to all local times
from AMPTE/CCE spacecraft observations on the dawn- and
dusksides of the inner magnetosphere spanning the $L$ value
range $L = 2.25$ to $6.75$. Observations by AMPTE/CCE of ring
current distributions over subsequent orbits during the storm
recovery phase are compared to model outputs. In the fol-

lowing, average flux means the average differential intensity (in $s^{-1}$ $cm^{-2}$ $sr^{-1}$ $keV^{-1}$) over pitch angles, except where another definition is specifically given.

The differential flux of ring current ions is a function of many variables, i.e., $L$ shell value, magnetic local time, energy, pitch angle, and elapsed time during the storm. Usually many plots are required to represent the whole picture of the distribution and its evolution. In this work, ion flux is visualized by a method we refer to as a chromogram, which uses color to display a function of three variables on a two-dimensional plot. Interesting features in the average flux, such as strong day-night asymmetry during injection, minimum in the energy spectrum, and other features controlled by energy dependence loss processes and drift, are manifested in the chromogram representation.

The evolutions of the pitch angle distribution of the ion fluxes during the storm recovery are also investigated. Calculated pitch angle distributions are fitted to $j(y) \propto (1 + Ay^n)$ to quantify the spatial, energy, species and temporal dependence, where $y$ is the sine of the equatorial pitch angle. A $y^n$ parameterization conveys particularly useful information because $n$ is a measure of pitch angle anisotropy [Williams et al., 1973; Roelof and Williams, 1988]. The results indicated substantial structuring of the spatial distribution of ring current ions that should be evident in global imagery as described by Williams et al. [1992].

## 2. The Model

Assuming a gyrotropic distribution and considering only losses due to charge exchange with neutral hydrogen and Coulomb drag interactions with the plasmasphere, the kinetic equation of the ring current species $s$ can be written as

$$\frac{\partial f_s}{\partial t} + \dot{R}_0 \frac{\partial f_s}{\partial R_0} + \dot{\phi} \frac{\partial f_s}{\partial \phi} + \dot{S} \frac{\partial f_s}{\partial S} = -v\sigma_s n_H f_s$$
$$+ \frac{1}{G}\frac{\partial}{\partial M}(\dot{M}Gf_s) + \frac{1}{G}\frac{\partial}{\partial K}(\dot{K}Gf_s) \qquad (1)$$

where $f_s(R_0, \phi, S, M, K)$ is the phase space distribution function, $R_0$ is the radial distance at the equator, $\phi$ is the magnetic local time, $S$ is the arc length along the magnetic field line, $M$ is the magnetic moment, and $K$ is defined as [McIlwain, 1966]

$$K \equiv J/(8m_s M)^{1/2} = \int_{S_m}^{S_m'} [B_m - B(S)]^{1/2} dS \qquad (2)$$

where $v$ is velocity, $\sigma_s$ is the cross section for charge exchange of species $s$ with the neutral hydrogen, $n_H$ is the hydrogen density, and $\dot{M}$ and $\dot{K}$ are the rates of change of $M$ and $K$, respectively, due to Coulomb interactions with the thermal plasmas. The expression of $\dot{M}$ is given in (20)–(21) in paper 1 and is repeated in the appendix. $K$ is an invariant variable in the case of zero parallel electric field [Roederer, 1970]. It is kept constant even with Coulomb interactions [Schulz and Lanzerotti, 1974]; therefore, the last term of the right-hand side of (1) is zero. $G$ is the Jacobian of the transformation $(x, y, z, v_x, v_y, v_z)$ to $(R_0, \phi, S, M, K)$ and is equal to

$$G = \frac{\pi B_0}{\mu T(y)}\left(\frac{8M}{m_s^3}\right)^{1/2} \qquad (3)$$

where $B_0$ is the equatorial magnetic field, $\mu$ is the cosine of the pitch angle, and $T(y)$ is a function of the sine of the equatorial pitch angle $y$ and is defined and approximated by Davidson [1976] as

$$T(y) \equiv \frac{1}{R_0}\int_0^{S_m}\frac{dS}{\mu} \qquad (4)$$
$$\approx 1.380173 - 0.639693 y^{0.75}$$

The derivation of $G$ is given in the appendix. The $y$ value can easily be calculated for given $M$ and $K$.

All models employed in this work are the same as those in paper 1. The magnetic field is assumed to be dipolar with the dipole axis coincident with the Earth's rotational axis. The convection electric field model is that of Volland-Stern [Volland, 1973; Stern, 1975], the plasmaspheric model is from Rasmussen et al. [1993], and the hydrogen density of Rairden et al. [1986] is used. The charge exchange cross sections are given by the work of Phaneuf et al. [1987] and Barnett [1990].

We multiply (1) by $1/\mu$ and integrate it along field line to obtain the bounce-averaged equation

$$\frac{\partial \bar{f}_s}{\partial t} + \langle \dot{R}_0 \rangle \frac{\partial \bar{f}_s}{\partial R_0} + \langle \dot{\phi} \rangle \frac{\partial \bar{f}_s}{\partial \phi} = -v\sigma_s \langle n_H \rangle \bar{f}_s$$
$$+ \frac{1}{M^{1/2}}\frac{\partial}{\partial M}\left(\langle \dot{M} \rangle M^{1/2} \bar{f}_s\right) \qquad (5)$$

where $\bar{f}_s$ is the average $f_s$ along the field line between mirror points. Since we are considering particles with bounce periods much shorter than the decay lifetime times, $f_s$ is assumed to be constant along field line and thus $\bar{f}_s$ can be replaced by the distribution function at the equator. The bounce-averaged value of $x$ is defined as

$$\langle x \rangle \equiv \int_{S_m}^{S_m'} x \frac{dS}{\mu} \Big/ \int_{S_m}^{S_m'}\frac{dS}{\mu}$$
$$= \frac{1}{2R_0 T(y)}\int_{S_m}^{S_m'} x \frac{dS}{\mu} \qquad (6)$$

The quantity $\dot{M}$ is constant over a bounce period because it is proportional to the plasmaspheric density, which is assumed to be constant along a field line.

Roederer [1970] showed that the $\mathbf{E} \times \mathbf{B}$ drift is independent of the position along a field line and can be represented by the values at the equator. The expression of $\mathbf{E} \times \mathbf{B}$ drift due to corotation and convection can be found in (16) and (17) in paper 1. The bounce-averaged gradient-curvature drift velocity in a dipolar field can be approximated by [Ejiri, 1978]

$$\langle \dot{\phi} \rangle_{gc} = \frac{-3M}{qR_0^2 y^2}\left(1 - \frac{I(y)}{6f(y)}\right) \qquad (7)$$

where the subscript $gc$ represents gradient-curvature drift. The functions $I(y)$ and $f(y)$ are given by Ejiri [1978] and are repeated here:

$$I(y) = 2\alpha(1-y) + 2\beta y \ln y + 4\beta(y - y^{1/2})$$
$$+ 3a_1(y^{1/3} - y) + 6a_2(y^{2/3} - y) \qquad (8a)$$
$$+ 6a_4(y - y^{4/3}) - 2a_3 y \ln y$$

$$f(y) = \alpha - \beta(y + y^{1/2}) + a_1 y^{1/3} + a_2 y^{2/3} + a_3 y + a_4 y^{4/3} \quad (8b)$$

where $\alpha = 1.38$, $\beta = 0.32$, $a_1 = 0.055$, $a_2 = -0.037$, $a_3 = -0.074$, and $a_4 = 0.056$. The function $[1 - I(y)/6f(y)]$ increases monotonically from 0.7 to 1 as $y$ goes from 0.05 to 1.

## 3. Initial Conditions at Minimum $Dst$ of Storm

After a complicated main phase of 2 days, the great storm in February 1986 attained a minimum $Dst$ of $-312$ nT on February 9, at about 0100 UT. The recovery is a typical two-phase process: a rapid initial recovery with an increase in $Dst$ of 140 nT in 6 hours, followed by a long slow recovery of tens of day. Differential flux ($s^{-1}$ $cm^{-2}$ $sr^{-1}$ $keV^{-1}$) of the bulk of the ring current (1–300 keV) just after minimum $Dst$, measured by the charge-energy-mass spectrometer (CHEM) [Gloeckler et al., 1985] that was carried aboard the Active Magnetospheric Particle Tracer Explorers/Charge Composition Explorer (AMPTE/CCE), is used to specify the initial conditions. Measurements during subsequent orbits are used to compare with the model outputs. The orbits of the CCE spacecraft are nearly equatorial with a 4.8° inclination and a period about 16 hours [Williams and Sugiura, 1985]. Particle fluxes are averaged at every 0.5 $R_E$ from $L$ shells of 2.25 to 6.75.

During the minimum $Dst$ of this storm, the inbound and outbound passes of the CCE orbit (orbit A) crossed the equator at about 1500 and 0700 LT, respectively. Figure 1 shows the $H^+$, average fluxes (symbols) taken from both passes during orbit A at $L \sim 2.3$ and $\sim 4.3$. At both $L$ shells ( Figures 1a and 1b), high-energy fluxes during outbound and inbound passes are similar to each other. Then at energies of 30–100 keV, the flux on the dawnside exceeds that on the duskside with the difference increasing with decreasing energy. Moreover, the energy at which fluxes from the two passes start to differ significantly is lower at $L = 4.3$ (Figure 1b) than at $L = 2.3$ (Figure 1a). The local time dependence of the initial distributions of $O^+$ and $He^+$, which are not shown, behaves in a similar manner to that of $H^+$. The local time asymmetry of ion distributions during the main phases of magnetic storms has been studied and observed [Roelof, 1987; Stüdemann et al., 1987]. The degree of asymmetry depends on the location and energy
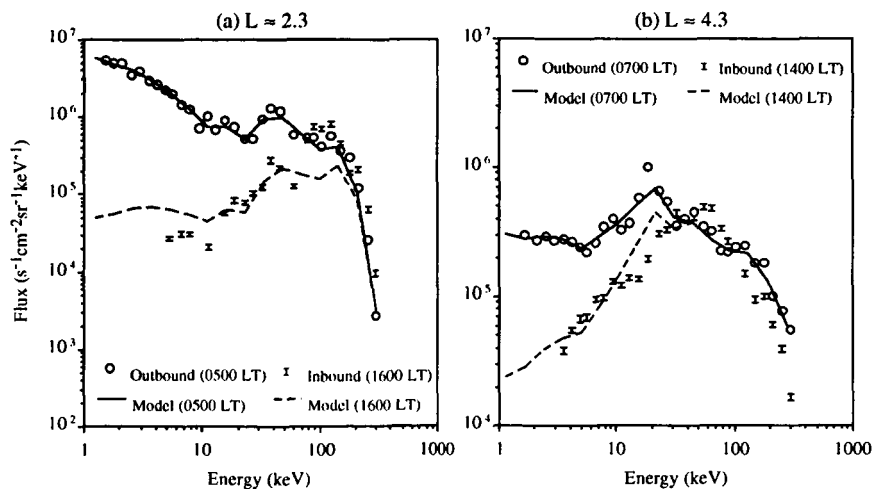
of the ions. Stüdemann et al. [1987] found the asymmetry between local evening and local morning became less pronounced at larger radial distances when they studied the ion distributions after the onset of a magnetic storm on May 2-3, 1986. Chen et al. [1993] studied the storm time transport of ring current and radiation belt ions. They found that the drift period of trapped ions with high energy ($M \geq 25$ MeV/G, $E \geq 280$ keV at $L = 3$) is short compared with the duration of the main phase of their model storm. Distributions of these particles should be fairly constant about local time by the end of the main phase. Also they found low-energy ($M \leq 10$ MeV/G, $E \leq 110$ keV at $L = 3$) ions are transported from open drift paths (plasma sheet) to closed drift paths (ring current) and the drift period in the ring current region exceeds the duration of the main phase. Therefore local time asymmetry of these particles at storm main phase is expected. Since the drift period for particles of a given energy is shorter at high $L$ than at low $L$ shell values, particle fluxes start to be symmetric with local time at lower energy as $L$ value increases. The CCE measurements presented in Figure 1 are consistent with the above arguments and observations.

Data from the outbound pass (at ~0300 UT, February 9) of orbit A are taken as initial conditions ($t = 0$) for $L = 2.25$–6.5 at 0500–0800 LT. The inbound pass of the same orbit is used as a guide to extrapolate the particle fluxes to all local times. Since the main phase of the February 1986 storm is comparatively long, local time symmetry can be reached for particles with lower energy than in the Chen et al. [1993] study of a shorter duration storm. In our study, ions with $M \geq 10$ MeV/G are assumed to be perfectly symmetric in local time at the time of minimum $Dst$ during the storm. For ions with lower magnetic moment, distributions are extrapolated in local time using the following expression:

$$f_s(\phi) = f_s(\phi_0) \exp\left[-(1 - \cos(\phi - \phi_0))/\sigma^2\right] \quad (9)$$

This fit gives a Gaussian distribution in local time around $\phi = \phi_0$, with variance equal to $\sigma^2$. We find that

$$\phi_0 = 0200 \text{ hour}$$

$$1/\sigma^2 = \frac{1}{0.8}\log\frac{10}{M} \quad M < 10 \text{ MeV} / \text{G} \quad (10)$$

$$1/\sigma^2 = 0 \quad M \geq 10 \text{ MeV} / \text{G}$$



**(a) L ≈ 2.3**

O Outbound (0500 LT)   x Inbound (1600 LT)

— Model (0500 LT)   – – Model (1600 LT)

Flux ($s^{-1}cm^{-2}sr^{-1}keV^{-1}$)

Energy (keV)

**(b) L ≈ 4.3**

O Outbound (0700 LT)   x Inbound (1400 LT)

— Model (0700 LT)   – – Model (1400 LT)

Energy (keV)

**Figure 1.** $H^+$ flux measured (symbols) at the inbound and outbound passes of the orbit at minimum $Dst$ of the February 1986 storm at (a) $L \sim 2.3$ and (b) $L \sim 4.3$. Solid lines are the initial condition based on the outbound data. Dashed lines are extrapolation at the same local time as the inbound data.

in order to have a best fit to the observations. The $f_s(\phi_o)$ value can be determined by the measurements during the outbound pass. Model initial H$^+$ fluxes at $L = 2.3$ and 4.3, at 0500 and 1600, and 0700 and 1500 LT, respectively, are overlaid with CCE measurements in Figure 1. As is shown by Figure 1, the approximation formulated in (10) is quite in agreement with measurements. The semiempirical "initial" (0300 UT, February 9) differential fluxes for the three major ion species (H$^+$, O$^+$, and He$^+$) at 0200 MLT are plotted in Figure 2. Particles are assumed to have isotropic pitch angle distribution initially at $t = 0$. Observations showed that pitch angle distributions during this time were not strongly peaked at 90° except at very small $L$ values [*Hamilton et al.*, 1988]. The total energy contained in the ring current is calculated by

$$E(\text{total}) = \sum_s \int \frac{1}{2} m_s v^2 f_s G' \, dR_o d\phi dM dK \qquad (11)$$

where $G' = 4\pi R_o B_o (2M/m_s^3)^{1/2}$. The derivation of $G'$ is also given in the appendix. Using (11), the initial energy contained in the ring current is found to be $3.30 \times 10^{31}$ keV. *Hamilton et al.* [1988] estimated the total energy at this pass and obtained a value of $4.15 \times 10^{31}$ keV. This is somewhat higher than we calculate because they have assumed isotropic distributions inside the whole flux tube at all local times.

The boundary conditions used are the same as those presented in paper 1 except for the upper boundary condition on $f_s$ at $L = 6.75$. A Dirichlet boundary condition (given $f_s$ at boundary) is used instead of a Neumann-type condition ($\partial f_s/\partial R_o = 0$). CCE ion flux data at $L = 6.75$ are taken as boundary values on the nightside throughout the storm. Particles are continuously injected from the plasma sheet to the injection boundary even during the recovery phase of a magnetic storm. Therefore the Dirichlet boundary condition allows the transmission of particle information from the tail to the ring current region during the storm. The boundary conditions are summarized and given as follows:

$$f_s(R_o < 2R_E) = 0, \qquad \langle \dot{R}_o \rangle > 0 \qquad (12a)$$

$$f_s(R_o = 6.75 R_E) = \text{CCE data}, \qquad \langle \dot{R}_o \rangle < 0 \qquad (12b)$$

$$f_s\left(\frac{1}{2} m_s v^2 > 317 \text{ keV}\right) = 0 \qquad (12c)$$

With the initial distribution and boundary conditions set up as specified, the initial value problem formulated in (5) can be solved numerically to obtain the phase space density at any time after the storm main phase.

## 4. Ring Current Fluxes During Storm Recovery

After 16 hours elapsed time, the calculated average flux is compared with measurements during the outbound pass of the next orbit (orbit B). Figure 3 displays the model results (solid lines) and the CCE data (symbols) with error bars at $L = 3.75$, 0600 MLT (Figure 3a) and at $L = 6.25$, 0800 MLT (Figure 3b). In both cases, the calculated fluxes of He$^+$ and O$^+$ agree fairly well with measurements. However, the calculated H$^+$ flux, at energies below 100 keV, is always greater than observations, indicating that other loss mechanisms, important for H$^+$, need to be included in the model. This overestimation of H$^+$ flux is also found at the subsequent orbit at 32 hours elapsed time.

Observational evidence indicates that loss of ring current ions through precipitation played an important role in the main and early recovery phases of the February 1986 storm. *Yeh and Foster* [1990] reported precipitating ion energy fluxes as high as 1 erg cm$^{-2}$ sr$^{-1}$ s$^{-1}$ for ions with $E < 32$ keV/$e$ over 48° to 58° IL during the 6-hour period 2000 UT on February 8 through 0200 UT on February 9. This IL interval mapped to the equatorial plane contained the maximum in the ring current energy density observed by AMPTE/CCE [*Hamilton et al.*, 1988]. During this same time interval, a rapid recovery of the surface magnetic field with an e-folding timescale of ~11 hours was seen in the *Dst* index. First results of a study of wave and particle signatures during this time interval were presented by *Kozyra et al.* [1994b] in which both a large amplitude Pc 5 wave and precipitation that peaked at energies consistent with resonant interactions with this wave were observed. The results of this study will be published separately.

Though there is discrepancy between calculated and observed low-energy (<100 keV) H$^+$ fluxes, our model can be used to illustrate general features in the temporal evolution of the ring current ion fluxes and the pitch angle distributions (section 6). To show the $L$ shell, magnetic local time, and energy dependence of the average flux on the same plot, a newly developed color display, designated as a chromogram, is used. The goal of a chromogram is to plot a function of three variables, $j(L, \phi, E)$, in a two-dimensional color plot. The dependence on the first two variables (i.e., $L$ and $\phi$) forms a pixel image in a two-dimensional $L$ - $\phi$ space, while the dependence
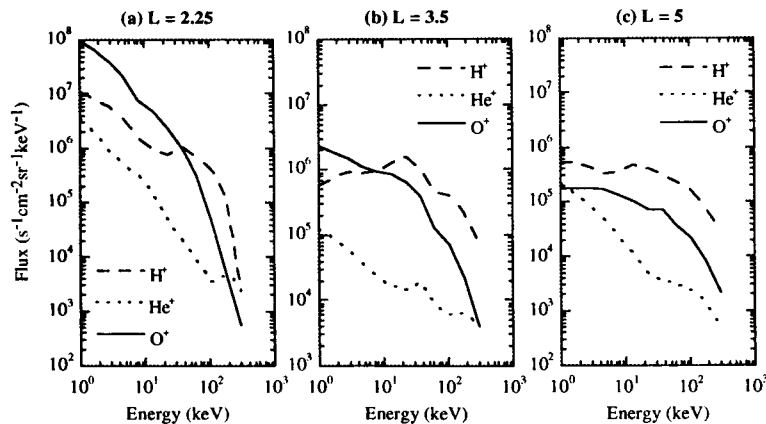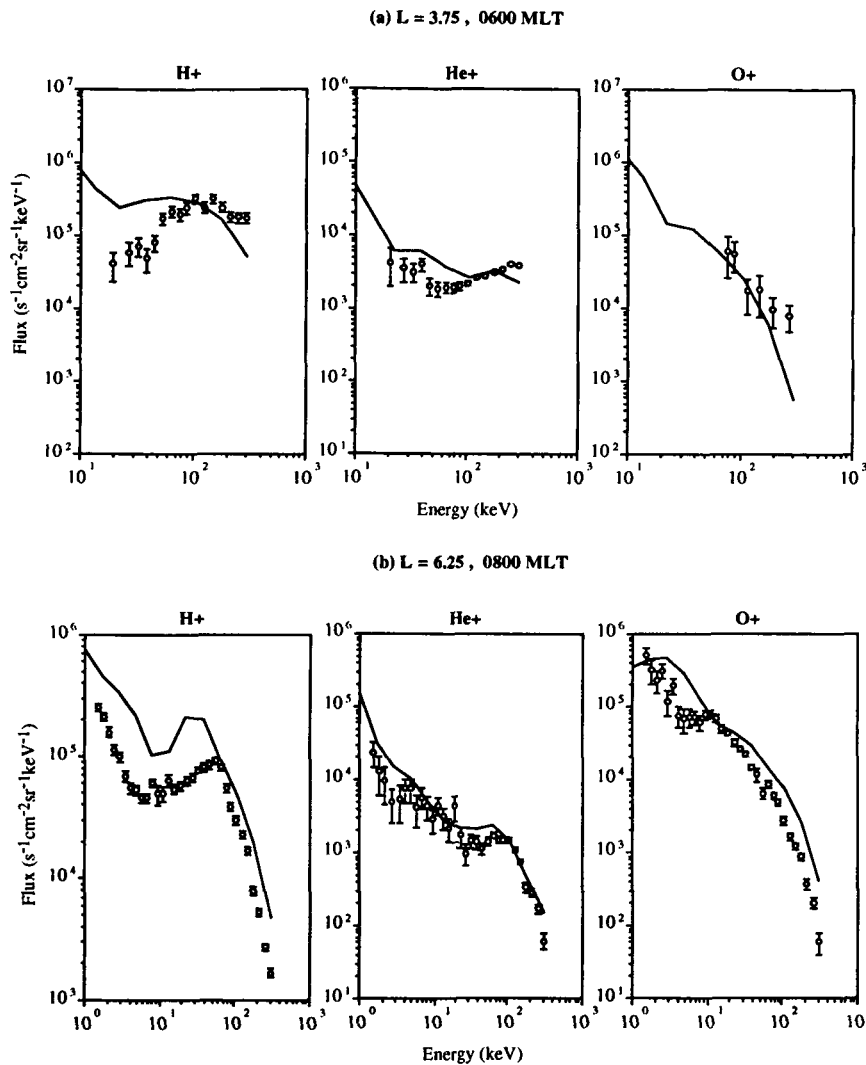


**Figure 2.** Initial differential flux of H$^+$, He$^+$, and O$^+$ at 0200 MLT at $L =$ (a) 2.25, (b) 3.5, and (c) 5.

**Figure 3.** The comparison of calculated flux (solid lines) with AMPTE/CCE measurement (symbols) at 16 hours after the storm main phase at (a) $L$ = 3.75, 0600 MLT and (b) $L$ = 6.25, 0800 MLT.

on the third variable ($E$) is encoded as color. The encoding of color uses the concept of three basic colors (photon energies) of light: red, green, and blue. Variable $E$ is divided into three ranges (Figure 4), associated with red ($R$), green ($G$), and blue ($B$), respectively. The average values of $j$ in these ranges are used to scale the $R$, $G$, $B$ components of the encoded color. The hue of the resulting color corresponds to the centroid or mean $E$ of $j(E)$; the saturation corresponds to the shape of $j(E)$; and the brightness corresponds to the average $j$ over the full range of $E$. Table 1 summarizes the interpretation of the color code. The rough energy distribution at each $L$ - $\phi$ location can be inferred from the color at that particular pixel. The detailed features of energy spectra cannot be resolved using the chromogram representation, but it is useful to indicate the spatial dependence of the energy distribution.

Using the chromogram representation, the average differential flux of $H^+$ is displayed in Plate 1 at selected times: $t$ = 0 (Plate 1a), $t$ = 5 hours (Plate 1b), and $t$ = 36 hours (Plate 1c) after the storm main phase. As shown in the color wheel, fluxes in energy ranges of 1–3 keV, 3–30 keV, and 30–100 keV are encoded with red, green, and blue, respectively. The gray-scale bar is a guide to the interpretation of brightness.

Isocontours of average (over the range of energy) fluxes are plotted to aid in distinguishing color from brightness. As mentioned in the last section, the initial distribution is peaked at and symmetric about 0200 MLT (Plate 1a). There is a strong day-night asymmetry in the initial ion fluxes. The enhanced low-energy population at $L$ = 2.3, shown in Figure 1a, is seen as the reddish region at the inner edge of the ring current in Plate 1a near dawn and dusk. Only high energy particles, which drift rapidly, can reach the dayside during storm injection, resulting in blue color (at lower brightness) on the dayside in the chromogram. Five hours later (Plate 1b), there is a clear separation of $H^+$ fluxes at different energies. Low-energy (<3 keV) $H^+$ ions corotate and drift from the nightside through dawn to the prenoon sector, while high energy (>30 keV) ions drift westward. At some intermediate energies, the westward gradient-curvature drift is comparable in magnitude with the eastward corotation, resulting in a nearly zero drift velocity. The purplish red at low $L$ is due to the overlapping of low- and high-energy ions which results in a double-peaked energy distribution. Medium-energy particles (green-cyan color) remain on the nightside injection region because of their small drift velocities. The lack of medium energy protons on the dayside
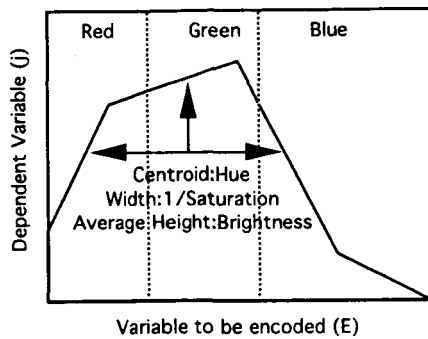
**Figure 4.** Curve $j(E)$ is divided into three subranges that are associated with red, green, and blue light, respectively.

corresponds to the well known "bite-out" in the dayside energy spectra [McIlwain, 1972; Lennartsson et al., 1981; Kistler et al., 1989]. The orange-brown fringes on the night-side outer boundary are the freshly injected low-energy ions.

As the storm recovery proceeds (Plate 1c), the low-energy population of $H^+$, which was injected close to the inner boundary during the main phase of the storm, is removed rapidly by charge exchange loss. Only high energy (>30 keV) $H^+$ remains in the low $L$ region. The quiescent convection field continues to push ions earthward on the nightside. The penetration distance varies with energy, with low-energy ions penetrating less deeply in $L$ [Ejiri et al., 1980]. As a consequence, another kind of separation of ions according to energy occurs during late recovery, as shown in Plate 1c at $t = 36$ hours. The magenta is the region where high- and low-energy particles coexist (again with a deficit at medium energies). The blue area represents the region forbidden to less energetic particles. The separation boundary, similar to a separatrix, is the boundary between open and closed drift paths for low-energy ions [Kivelson et al., 1980]. If the convection field is constant with time and oriented dawn to dusk, the trajectories of the cold ions are symmetric about the dawn-dusk axis, having the tip (sharp point) of the separatrix located at dusk. This kind of separatrix starts to be seen about 1 day after the main phase, and the tip is at about 1500 MLT. The separatrix then swings back and forth in the post-noon sector. Figure 5 plots the position of the tip in MLT during the storm, together with the $Kp$ values during storm recovery. It is interesting to see that when $Kp$ is decreasing, the separatrix rotates toward the dusk; the separatrix turns westward if $Kp$ is increasing. This oscillation of the separatrix is a result of the competition between corotation and convection. When convection is strong (indicated by increasing $Kp$), particles drift quickly outward and are lost at the dayside magnetopause near noon. At lower $Kp$, the corotation is relatively strong and bends the particle trajectory toward the duskside. The motion of the separatrix in response to the $Kp$ index described above is consistent with the $Kp$ dependence of the plasmapause location, based on the empirical model of D. L. Gallagher (private communication, 1994).

The temporal evolutions of $O^+$ and $He^+$ fluxes are similar to each other but quite different from that of $H^+$ because their charge exchange lifetime is long at low energies and short at high energies, in contrast to that of $H^+$. At the early recovery, the separation of particles with different energies, as shown in Plate 1b, is also seen for these heavy ions. As the storm recovery proceeds, high energy $O^+$ and $He^+$, which are initially at low $L$, are significantly removed by charge exchange loss.

Only low-energy heavy ions are left at small $L$. The slowly drifting medium energy $O^+$ and $He^+$ eventually reach all local times at $L$ of 3–5 in about 1 day without significant charge exchange loss. The outer region is mainly occupied by the freshly injected low-energy ions. Plate 1d is the chromogram representation of $O^+$ flux at $t = 36$ hours. As shown in the plot, during late recovery, instead of a separatrix, bands of fairly symmetric heavy ions of different energies are formed. The yellow band at dawn and in the prenoon sector corresponds to the existence of low-energy ions in a background of medium energy particles. These low-energy $O^+$ ions were convected, following the storm injection, deeply into $L \sim 2.3$. During the recovery phase of the storm, the drift of these ions is dominated by corotation out to increasing radial distances due to the decreasing convection field, indicated by $Kp$.

## 5. Drift Hole in the Energy Spectra

A dip or sharp drop-off in the ion energy spectra at low energies ($1 \le E \le 10$ keV) is a consistent feature in observations. A deep minimum was always found in the proton spectra observed by geosynchronous satellite ATS 5 [McIlwain, 1972]. The dip was seen at a wide range of local time: 0200–1800 hours and the energy of the minimum decreased with local time. Lennartsson et al. [1981] used data from the plasma composition experiment on ISEE 1 and reported a hole in the ion ($O^+$, $H^+$, and $He^+$) phase space density at ~3.5 keV, at 4–5 $R_E$ and LT 11.6–12.1 hours, during a magnetic storm on day 329/78, which was one of the 10 storms selected. Ions of certain energies, experience eastward and westward drifts that are similar in magnitude, resulting in very slow drift velocity. The hole in the energy spectra corresponds to particles at these energies which have either not yet reached the observation point or which have experienced significant losses during their slow drift to the observation point.

Theoretical modeling reproduces the hole observed in measurements. McIlwain [1972] studied the drift paths of ring current ions and interpreted the minima in the proton spectra as due to particles whose computed trajectories penetrate to the highest magnetic field value and thus have the longest travel time. He predicted a negative correlation between the energy of the minima and local time. His results were consistent with observations by ATS 5. Kistler et al. [1989] did a similar calculations for $L$ values of 3.5 to 5.5, using different electric field model parameters. They also found a negative slope in energy of the minimum versus local time and the slope was steeper with increasing $Kp$. Dips and sharp drop offs were also reproduced in our previous study (paper 1). We found that dips in the prenoon sector were at higher energies than those in the postnoon sector, consistent with the calculation of Kistler et

**Table 1.** Guide to the Interpretation of Chromogram Color

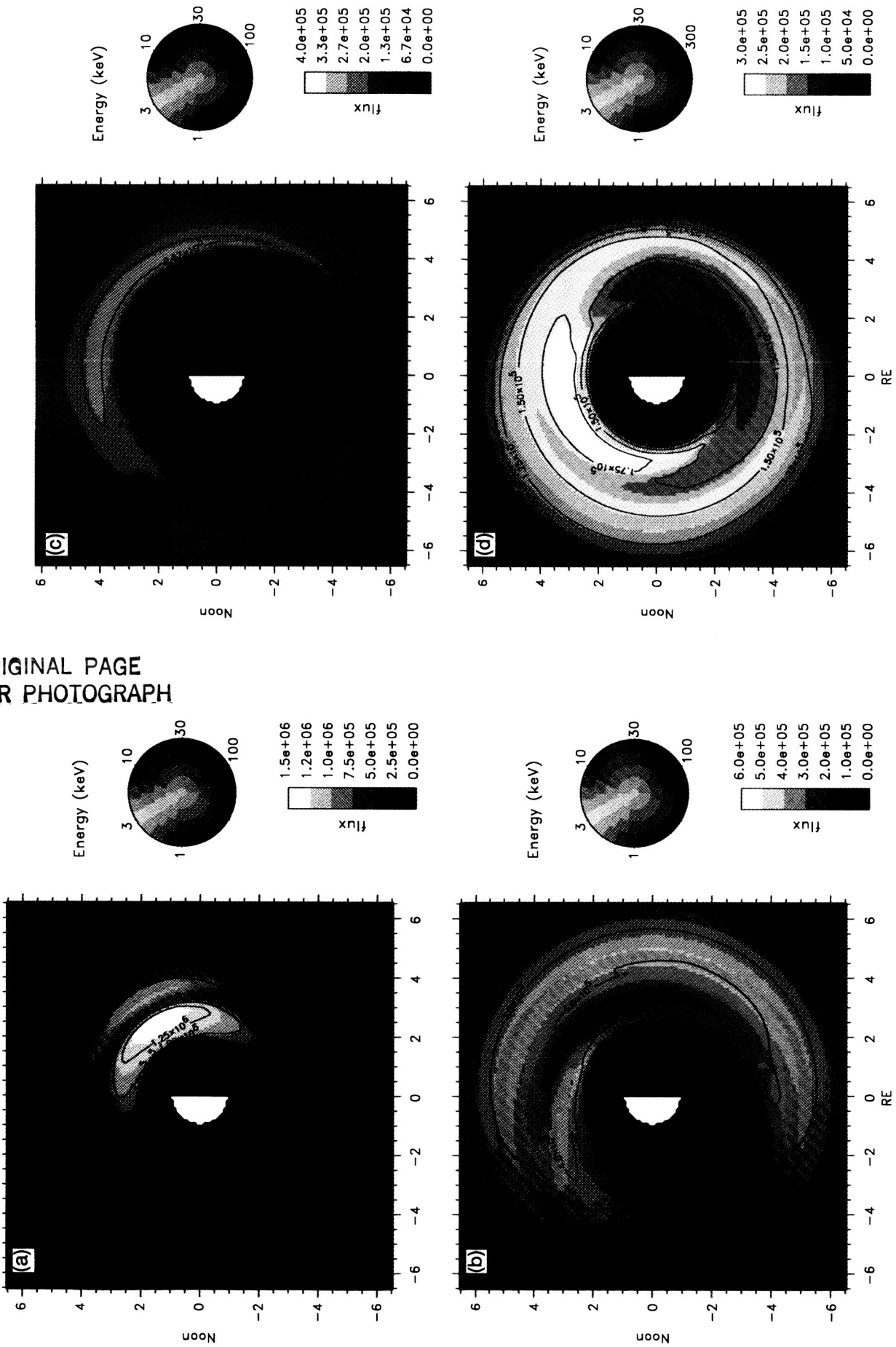| Color | Interpretation |
|---|---|
| gray | no dependence on $E$(flat) |
| red | strongly peaked at low value of $E$ |
| green | strongly peaked at midscale in $E$ |
| blue | strongly peaked at high values of $E$ |
| yellow | weakly peaked toward low $E$ |
| cyan | weakly peaked toward high $E$ |
| magenta | peaked at high and low $E$ |

**Plate 1.** Chromogram representation of the average flux of H$^+$ in [s$^{-1}$ cm$^{-2}$ sr$^{-1}$ keV$^{-1}$] at (a) $t = 0$, (b) $t = 5$ hours, (c) $t = 36$ hours, and (d) average flux of O$^+$ at $t = 36$ hours.
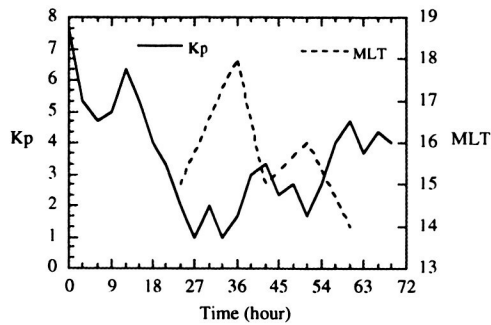
**Figure 5.** The position of the tip of the separatrix in MLT and $Kp$ values as a function of elapsed time during the storm.

*al.* [1989]. In addition, the dip was more pronounced in the postnoon sector than in the prenoon sector. These features in the hole can be easily explained by the drift motion. Let the energy at which drift velocity is zero be $E_0$. Ions with energy slightly less than $E_0$ drift slowly from the nightside in eastward direction and reach dawn and then the prenoon sector. In contrast, ions with energy slightly larger than $E_0$ drift slowly through the duskside. As a result, the energy of the minima in the prenoon sector is higher than in the postnoon sector.

Holes in the energy spectra are also evident in displays of the average flux presented in the last section. At $t = 5$ hours (Plate 1b), dips at medium energies (3–30 keV) in the dayside $H^+$ spectra are obvious because medium energy particles are found only on the nightside. During quiet period, as shown in Plate 1c, region of magenta color represents peaks in the ion

distribution at both high and low energies and this corresponds to a dip at medium energies. In other words, holes in the energy spectra should be seen over almost all local times at the geosynchronous orbit and over a restricted local time interval at lower $L$ shells.

In order to better visualize the variation of the drift hole with energy and local time, a chromogram representation of the average flux, similar to those shown in Plate 1, is presented. However, at this time, the $L$ shell dependence of average flux is encoded as color, while energy and local time span the two-dimensional plot. Using the same token as energy encoding, red color represents flux peaking at low $L$ values, blue represents peak flux at high $L$, etc. In this orientation, for a given local time, the energy of the minimum flux (if there is one) can be easily identified. Plate 2 displays the logarithm of the average flux of $H^+$ as a function of energy and local time with $L$ shell color encoded at $t = 5$ hours. Isocontours of average flux, over the range of $L$ shell, are overlaid on the plot. The hole feature forms at 2 hours after the storm main phase. The beak shape of the minimum flux region is seen on the dayside at energies <30 keV. The energy of the minimum in the prenoon sector is higher than that in the post-noon sector, as expected. The "beak" is, in general, blue in color, indicating that the hole is more pronounced at low $L$ values. As the storm recovery proceeds, the beak extends toward predawn and duskside. This hole structure persists throughout the storm.

Drift holes are also found in the energy spectra of $O^+$ and $He^+$ but they are not as deep as the ones in the proton distribution. The charge exchange lifetimes of low-energy $O^+$ and $He^+$ are very long and are on the order of days to tens of day [*Fok et*
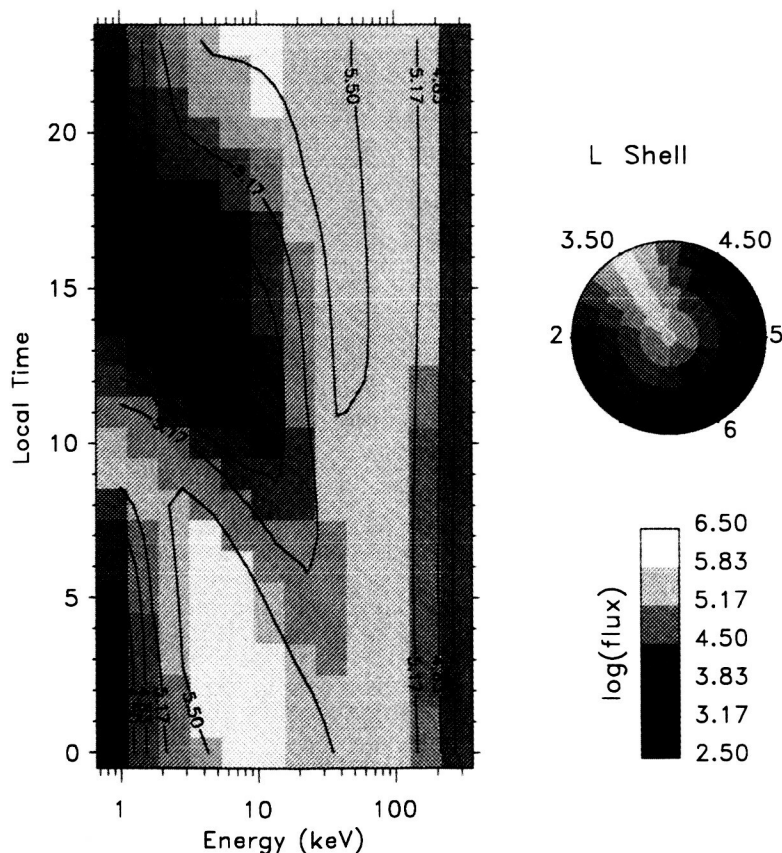


**Plate 2.** Chromogram representation of the "hole" in the energy spectra of $H^+$. $L$ dependence of log(flux) is color encoded.

al., 1991]. $O^+$ and $He^+$ ions with small drift velocity could gradually reach the dayside, without significant loss due to charge exchange with the hydrogen geocorona. Sluggish $O^+$ and $He^+$ fill the hole region during late recovery phase (Plate 1d).

A minimum in the ring current ion energy spectra due to wave-particle interactions has also been observed. *Williams et al.* [1973], using measurement from Explorer 45, found a dip in the proton energy spectra at 40–80 keV and $L$ shells of 3–4 during a storm in December 1971. The authors examined the pitch angle anisotropy of the proton fluxes and showed that they were consistent with the initiation of the ion-cyclotron instability. Dips in the energy spectra due to drift motion can easily be distinguished from those that result from wave-particle interactions. Ions of different species, but with same energy and charge state, drift along identical trajectories. The energy at which the drift hole occurs, corresponding to particles with the longest drift period, is independent of species and should appear in the distributions of all species [*Lennartsson et al.*, 1981; *Kistler et al.*, 1989; paper 1].

## 6. Pitch Angle Distribution

During the main phase of a magnetic storm, ring current particles are convected earthward from the tail to the inner magnetosphere. These fleshly injected particles are roughly pitch angle isotropic. As they are trapped in the inner magnetosphere, particles with different pitch angles bounce and drift differently. Particles with small equatorial pitch angles ($\alpha_0$) have mirror points at low altitude and experience large charge exchange losses. The anisotropy in pitch angle distribution increases as the storm recovery proceeds.

The modeled pitch angle distributions during the recovery phase of the storm have been fitted by a three-variable function in order to quantify their temporal evolution. The function of fit is of the form used by *Roelof et al.* [1992],

$$j(y) = j_0(1 + Ay^n) \qquad (13)$$

where $j$ is the differential flux, $j_0$ is a constant that does not depend on pitch angle, and $A$ and $n$ are the linear and exponential index, respectively, for the pitch angle distribution. $n$ is expected to be positive (flux peaked at 90°) if charge exchange is the dominant process. The pitch angle anisotropy, indicated by $n$, is higher at low $L$ shells, where hydrogen density is large, than at high $L$. In some cases, $n$ may be negative if the drift motion at some particular energies results in the more rapid movement of particles with small pitch angles into certain locations. Figure 6 gives two examples of differential flux as a function of $y$ calculated from the model and the corresponding fits, showing both the cases of positive and negative $n$. $j_0 A$ can be considered to be the quantity reflecting the average flux over pitch angle.

The parameter $n$ is assumed to be zero at the beginning of the recovery phase ($t = 0$). The variation of $n$ with time for ring current $O^+$ at four selected energies: 1.7, 8.0, 22.4, and 106 keV is examined next. The reason for choosing $O^+$ to demonstrate the temporal variation of $n$ is to separate the effect of drift motion from that of charge exchange loss on the pitch angle distribution. The charge exchange lifetime of $O^+$ decreases as energy increases. At low energies (<10 keV), where charge exchange loss is weak, and the lifetime is on the order of days [*Fok et al.*, 1991], corotation competes with
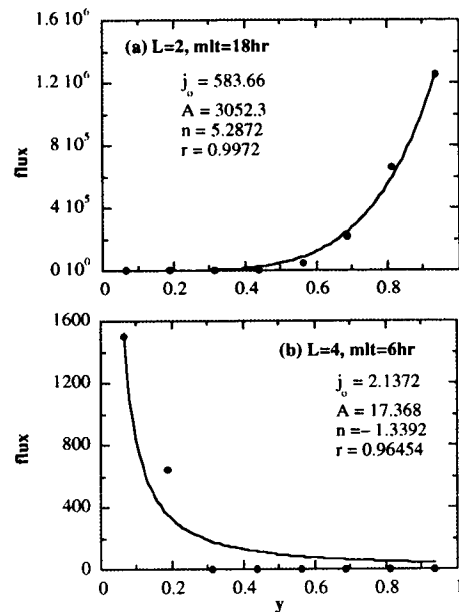


**Figure 6.** Calculated fluxes (symbols) overlaid with the fit (solid lines), $j = j_0(1 + Ay^n)$. Data are taken from the calculated $O^+$ flux at $t = 16$ hours at (a) $L = 2$, 1800 MLT and (b) $L = 4$, 0600 MLT. $r$ is the correlation coefficient of the fit to the data.

westward drift, which is pitch angle dependent. Low-energy ions with the same energy but different pitch angles may drift in opposite directions. Therefore the pitch angle distribution at these energies is mainly determined by drift motion. For energies greater than about 20 keV, particles drift rapidly in the westward direction with a period of hours regardless of pitch angle. The pitch angle distribution of these ions is thus shaped by charge exchange loss only.

Plate 3 displays the values of $n$ for $O^+$ at selected energies, at different $L$ shells and magnetic local times at 6 hours (Plate 3a) and 36 hours (Plate 3b) after the storm main phase. At $t = 6$ hours, the contours of constant $n$ for 106.3 keV $O^+$ are quite symmetric with local time and their magnitude decreases with increasing $L$. At $L \sim 2$, the pitch angle distribution is strongly peak at 90° with $n$ greater than 4. For 8 keV and 22.4 keV $O^+$, $n$ is approximately equal to 2 at low $L$ values and is between 0 and 1 at high $L$. The irregular features (i.e., the thin blue strip at $E = 8$ keV, $L = 4.7$, nightside) on the contours are drift effects. At low energy (1.7 keV $O^+$), there is a thick band of negative $n$ stretching from the duskside through midnight to the dawnside at $L$ of 3 to 5, where the motion of particles at this energy is dominated by corotation. In order to understand why fewer particles with large pitch angles populate this part of magnetosphere, the drift paths of ions of 90° equatorial pitch angle and energy at 1.7 keV at $L = 4$ are shown in Figure 7. The maximum plotting time is 6 hours. As shown in the figure, ions drifting in from the nightside boundary barely reach an $L$ shell of 4 in 6 hours. Particles of the same energy but small $y$ have weaker westward gradient-curvature drift (7). As a result the net eastward drift of particles with small pitch angles is faster than that of particles with large pitch angles. In 6 hours, ions with small pitch angles can better reach the nightside at $L$ shells ranging from 3 to 5, and thus the index $n$ is negative in this region at this particular time. This band of negative $n$ is also seen in the pitch angle distributions of $H^+$ and $He^+$.

As the recovery of the storm continues, the pitch angle anisotropy increases. At $t = 36$ hours (Plate 3b), $n$ attains a
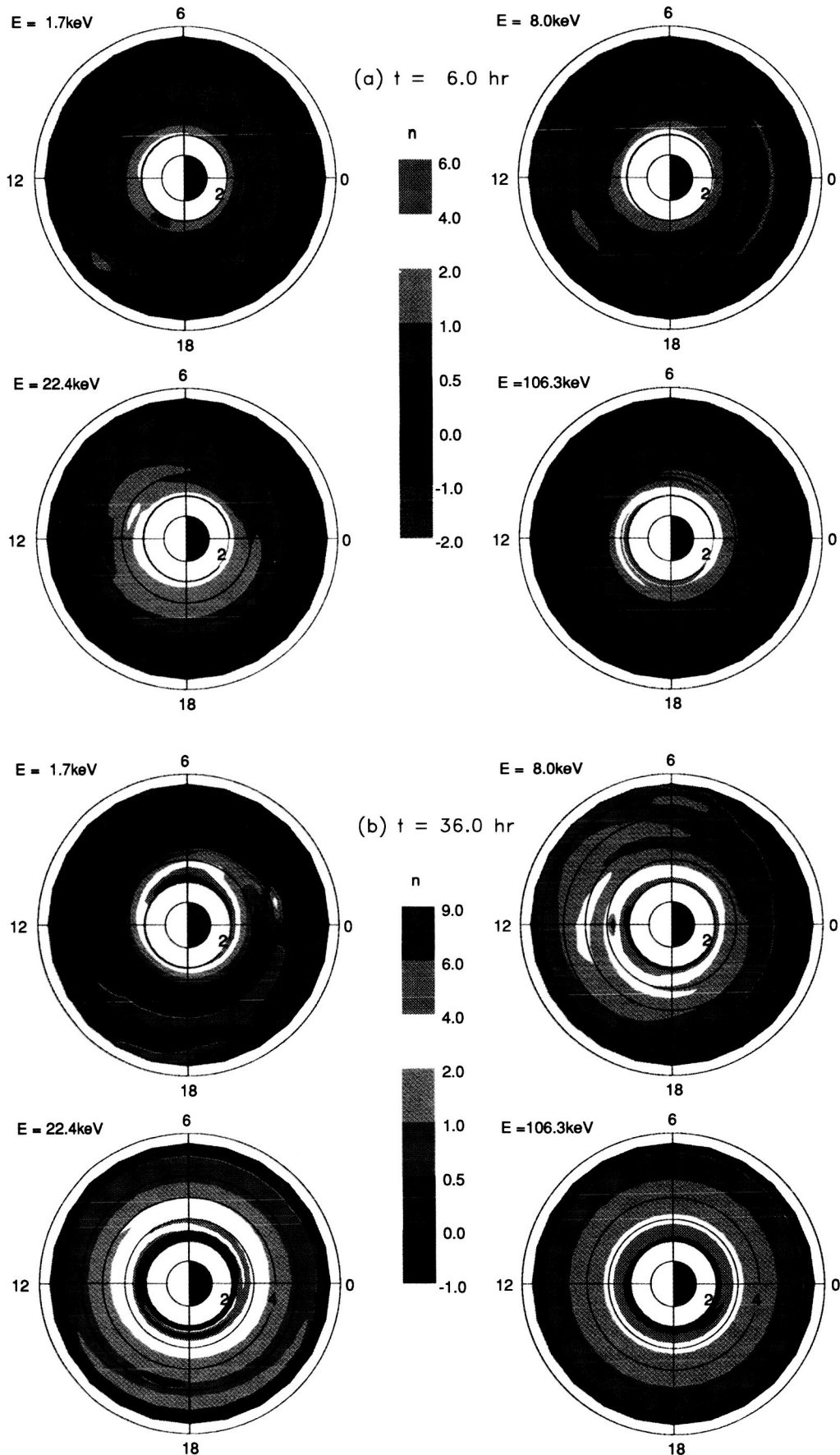
**Plate 3.** Exponential index of pitch angle distribution, $n$, of $O^+$ at four selected energies at (a) $t = 6$ hours and (b) $t = 36$ hours.

Symbols are plotted at every 30. minutes
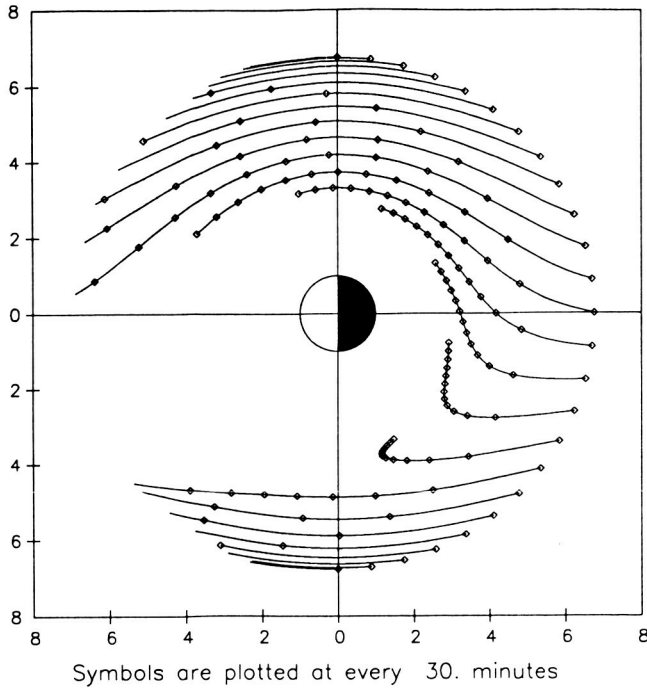
**Figure 7.** Drift paths of equatorially mirroring particles injected from the nightside boundary. Particle energy is 1.7 keV at $L = 4$ and the maximum plotting time is 6 hours.

value larger than 6 at $L \sim 2$ for all energies. The band of negative $n$ at 1.7 keV rotates and spans from 0100 to 1200 MLT with smaller negative values ($n > -1$) than those at 6 hours elapsed time. Features in the pitch angle distributions can also

be seen in the spatial distribution along field lines. Positive $n$ corresponds to maximum flux near the equator, while negative $n$ indicates strong flux at high latitudes. A chromogram of the average flux of $O^+$ in the X-Z plane at 36 hours is given in Plate 4. This is a meridian view of Plate 1d. In general, ion fluxes are peaked near the equator. This is particularly obvious, in this case, on the dayside at $L < 3.5$. As shown in Plate 4, higher fluxes of low energy (reddish) than higher energy (green) $O^+$ are visible at high latitudes as a consequence of the smaller charge exchange loss of $O^+$ ions at low energies. The strong fluxes at high latitudes on the dayside at $L \sim 4.5$ result from differences in the drifts experienced by ions with small pitch angle as compared to ions with large pitch angles at that particular location (negative $n$ region at energies less than 8 keV shown in Plate 3b). Unfortunately, no pitch angle information from measurement is available to compare with the model distributions during the recovery phase as the background radiation was strong.

Features in the pitch angle distributions of $H^+$ and $He^+$, which are not shown here, can be understood using physical insights gained from examination of the $O^+$ distribution. $n$ for 1.7 keV $H^+$ reaches a high value of 15 at $L \sim 2$, 12 hours after the injection. For 106 keV $H^+$, $n$ is never larger than 3 because its charge exchange lifetime is long, on the order of 10 days. $He^+$ behaves in a similar manner to $O^+$. However, in general, $n$ for the $He^+$ distribution has lower values than that for $O^+$ due to the longer charge exchange lifetime of $He^+$.

## 7. Discussion

A three-dimensional ring current model has been developed to study the temporal evolution of particle fluxes and the pitch
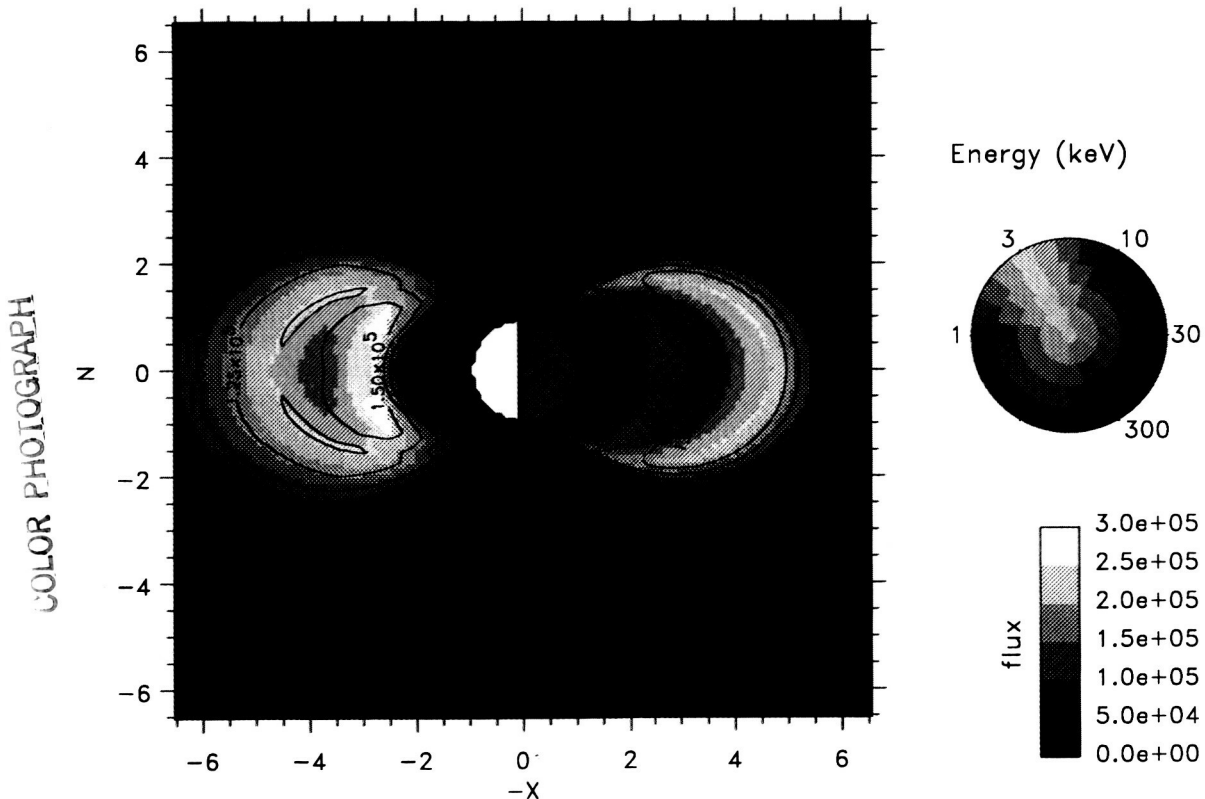


**Plate 4.** Chromogram of the average flux of $O^+$ in [$s^{-1}$ $cm^{-2}$ $sr^{-1}$ $keV^{-1}$] at $t = 36$ hours on the X-Z plane, which is the meridian view of Plate 1d.

angle distribution for the three ring current major ion species: $H^+$, $He^+$, and $O^+$. Under the assumption of constant differential flux along field lines, ring current distribution in the inner magnetosphere can be represented by the values at the equator.

Scattering of ions into the atmospheric loss cone during resonant interactions with plasma waves (not included in the present model) may make a significant contribution to ring current loss particularly during the main and early recovery phases of a magnetic storm. Williams et al. [1973] found dips in the energy spectra at ~40–80 keV from the proton detector experiment flown onboard Explorer 45. Pitch angle diffusion of ring current protons during resonant interactions with ion cyclotron waves was proposed to account for the loss of the protons and the subsequent formation of dips in the distribution. The general role of ion cyclotron waves in ring current decay, however, is unclear. Anderson et al. [1992] reported that large amplitude ($\delta B > 0.8\ \gamma$) ion cyclotron waves are rare in the inner magnetosphere ($L \leq 5$), appearing in the AMPTE/CCE data less than 1% of the time regardless of local time. Other plasma wave interactions under study in the ring current region involve Pc 5 waves [Li et al., 1993], lower hybrid waves [LaBelle and Treumann, 1988; Roth et al., 1990], and plasmaspheric hiss [Kozyra et al., 1994a].

In Figure 8, the total energy contained in the ring current as a function of the storm elapsed time is plotted and compared with the measured Dst values during the storm recovery. The calculated total energy decreases at a comparative steady rate, different from the observed two-step process, which consists of a rapid initial recovery followed by a relatively slow increase of Dst. Hamilton et al. [1988] suggested that the rapid charge exchange loss of 75–100 keV $O^+$ at $L \sim 3$ was responsible for the initial phase of recovery. However, the Kp index, which is used to parameterize the convection field intensity and thus the energization strength, is still high (>5) during the early recovery. Therefore, the energization of the continuously injected ions compensates the decrease in energy due to charge exchange losses. The convection model we used does not allow the ring current system to relax and recover shortly after the storm main phase. Gonzalez et al. [1994] suggested that the efficiency of energy injection into the ring current is higher during main phase than during nonmain phase, even at the same level of geomagnetic activity. Our model may overestimate the energization force during the storm recovery and thus cannot reproduce the initial rapid recovery. Another loss
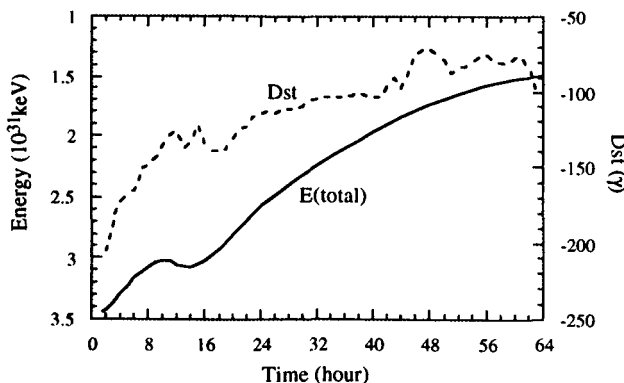
process, such as wave-particle interaction, is also a candidate in producing the rapid decay. As shown in Figure 3a, in which the calculated $H^+$ flux is compared with observation, including only charge exchange and Coulomb losses can not explain the decrease in $H^+$ flux at low energies (<100 keV). This problem should be re-addressed when a convection model with storm-phase dependent efficiency and enough information on wave measurement or particle precipitation are available.

The chromogram helps to reveal the ring current dynamics. With energy distribution encoded in color, spatial and energy dependence of the particle flux can be put on a two-dimensional plot. The strong day-night asymmetry in the injection, the separation of particles of different energies, the minimum in energy spectra, and other known features of ring current are qualitatively and quantitatively displayed using chromograms. Moreover, the region corresponds to a cutoff of low energies $H^+$ during quiet periods, predicted in this work, has never been addressed. If the time sequence of the chromogram is presented in a movie, the evolution of storm time ring current in space and energy will be vividly shown. This is one future goal of the present study. The chromogram is also an informative representation of the hole feature in the energy spectra. The calculated local time and energy dependence of the minimum in this study are generally consistent with the work of McIlwain [1972] and Kistler et al. [1989]. Also, the L shell dependence of the hole is encoded with color and displayed in a chromogram format. This plot demonstrates that holes are deeper at low L values.

The pitch angle distribution is well fit by the function $j = j_0 (1 + Ay^n)$. The correlation is always over 0.9. This work is the first attempt to calculate $n$ and $A$ for every energy and species, at any location in the ring current region. The complete pitch angle distribution can be estimated by these two indices if it is not given by data. For instance, if only $j(\pi/2)$ is measured, the flux at other pitch angles can be obtained by $j(y) = j(\pi/2)(1 + Ay^n)/(1 + A)$. In case of average flux, $<j>$, being measured, $j(y)$ is given by: $<j>(1 + Ay^n)/(1 + A<y^n>)$, where $<y^n>$ can be expressed as [Roelof, private communication, 1994]

$$\left\langle y^n \right\rangle = \frac{1}{2}\int_0^\pi d\alpha_0 \sin^{n+1}\alpha_0 = \frac{\sqrt{\pi}}{2} \frac{\Gamma\left(\frac{n}{2}+1\right)}{\Gamma\left(\frac{n}{2}+\frac{3}{2}\right)} \qquad n > -2 \qquad (14)$$

The spatial distribution of ring current ions along field lines, presented in this work, provides information useful in three-dimensional magnetospheric imagery, such as the global imaging of ring current using energetic neutral atoms [Roelof and William, 1988; 1990].

## 8. Conclusions

A three-dimensional ring current model has been developed to study the evolution of ion flux intensities and pitch angle distributions during the recovery phase of a magnetic storm similar to the major storm in February 1986. Our major results are listed as follows:

1. By bounce averaging the kinetic equation of the ion distribution function, the flux intensity and pitch angle distribution along a field line can be inferred from the information at a reference point (usually at the equator) on the field line.

2. The model generally reproduces the measured fluxes of the three major ring current ion species ($H^+$, $O^+$, and $He^+$).



Figure 8. Calculated total ring current energy and the observed Dst as a function of elapsed time during the storm recovery.

However, the calculation always over estimates the $H^+$ fluxes at energies below 100 keV. The exclusion of wave-particle interactions in the present model is believed to be responsible for this discrepancy.

3. A chromogram is a new idea for data visualization. Interesting features in the storm-time ring current ions, such as day-night asymmetry during injection, separation of ions at different energies due to difference in drift velocities, drift hole on the dayside at energies below 10 keV, energy and species dependence on charge exchange lifetimes, and spatial distribution along field lines, are clearly shown using the chromogram representation.

4. The pitch angle distribution of ion flux is well fit by the function $j_0(1 + Ay^n)$. At late recovery, parameter $n$ can reach a value of 6 or higher at the inner edge of the ring current for species with strong charge exchange loss (i.e., $O^+$ ion, and $H^+$ ion at energy <50 keV). A negative $n$ region is found, as a drift effect, at $L \sim 4$ at low energy (<8 keV) for all species.

This current model cannot be used to model the main phase development of magnetic storm since the magnetic field and electric field model employed are oversimplified. We plan to use more realistic models for magnetic and electric fields in order to simulate injection processes of storms. The effects on ring current evolution due to wave-particle interactions will also be included in our future work.

## Appendix

1. Expression of $\dot{M}$: The expression of $\dot{M}$ is given in (20)–(21) in paper 1 and is repeated here:

$$\dot{M} = \frac{dM}{dt} = -\frac{2M\Gamma_s}{v^3}\sum_b <n_b> Z_b^2$$
$$\left[\frac{2v^2}{v_b^2}\left(1+\frac{m_s}{m_b}\right)G\left(\frac{v}{v_b}\right) - erf\left(\frac{v}{v_b}\right)\right]$$

(A1)

where $\Gamma_s = \dfrac{Z_s^2 e^4 \ln \Lambda}{4\pi \varepsilon_0^2 m_s^2}$

$b$      plasmaspheric $e^-$, $H^+$, $He^+$, or $O^+$;

$\ln \Lambda$      Coulomb logarithm;

$Z_b e$, $Z_s e$      charge of species $b$ and $s$;

$<n_b>$      the bounce-averaged density of plasmaspheric species $b$;

$v_b$      thermal velocity of $b$;

$G(x) = \dfrac{erf(x) - x\, erf'(x)}{2x^2}$

2. Jacobian $G$ and $G'$: The Jacobian $G$ is a function such that,

$$\frac{1}{G} = \frac{dR_o d\phi dS dM dK}{d^3 r d^3 v}$$

(A2)

The differential volume $d^3r$ along a flux tube can be expressed as: $(B_o/B)R_o dR_o d\phi dS$. In the guiding center approximation, the motion of a particle can be characterized by the velocity components parallel ($v_\parallel$) and the perpendicular ($v_\perp$) to the magnetic field. $d^3v$ thus can be written as: $2 \times (2\pi v_\perp dv_\parallel dv_\perp)$.

The factor of 2 comes from the assumption that $f_s(v_\parallel) = f_s(-v_\parallel)$ and $v_\parallel$ goes from 0 to $\infty$. Putting the expressions of $d^3r$ and $d^3v$ into (A2), we have

$$\frac{1}{G} = \frac{B}{4\pi v_\perp R_o B_o}\frac{dMdK}{dv_\parallel dv_\perp}$$

$$= \frac{B}{4\pi v_\perp R_o B_o}\begin{vmatrix}\left(\frac{\partial M}{\partial v_\parallel}\right)_{v_\perp} & \left(\frac{\partial K}{\partial v_\parallel}\right)_{v_\perp} \\ \left(\frac{\partial M}{\partial v_\perp}\right)_{v_\parallel} & \left(\frac{\partial K}{\partial v_\perp}\right)_{v_\parallel}\end{vmatrix}$$

(A3)

It can be shown that

$$\left(\frac{\partial M}{\partial v_\parallel}\right)_{v_\perp} = 0$$

$$\left(\frac{\partial M}{\partial v_\perp}\right)_{v_\parallel} = \frac{m_s v_\perp}{B}$$

(A4)

$$\left(\frac{\partial K}{\partial v_\parallel}\right)_{v_\perp} = \mu R_o T(y)\sqrt{\frac{2m_s}{M}}$$

Thus $G$ has the expression as was given in (3).

The total number of species $s$ is given by

$$N_s = \int \cdots \int f_s \frac{\pi B_o}{\mu T(y)}\left(\frac{8M}{m_s^3}\right)^{1/2} dS dR_o d\phi dM dK$$

$$= \int \cdots \left(\int_{S_m}^{S_m'} \frac{f_s dS}{\mu}\right)\frac{\pi B_o}{T(y)}\left(\frac{8M}{m_s^3}\right)^{1/2} dR_o d\phi dM dK$$

(A5)

$$= \int \cdots \int \bar{f}_s 2R_o\pi B_o\left(\frac{8M}{m_s^3}\right)^{1/2} dR_o d\phi dM dK$$

$$= \int \cdots \int \bar{f}_s G' dR_o d\phi dM dK$$

where $G' = 4\pi R_o B_o(2M/m_s^3)^{1/2}$.

## References

Anderson, B. J., R. E. Erlandson, and L. J. Zanetti, A statistical study of Pc 1-2 magnetic pulsations in the equatorial magnetosphere, 1, Equatorial occurrence distributions, *J. Geophys. Res., 97*, 3075-3088, 1992.

Barnett, C. F., Atomic data for fusion, Vol. 1, Collisions of H, $H_2$, He and Li atoms and ions with atoms and molecules, *Tech. Rep. ORNL-6086/V1*, Oak Ridge Nat. Lab., Oak Ridge, Tenn., 1990.

Chen, M. W., M. Schulz, L. R. Lyons, and D. J. Gorney, Stormtime transport of ring current and radiation belt ions, *J. Geophys. Res., 98*, 3835-3849, 1993.

Chen, M. W., M. Schulz, and L. R. Lyons, Simulations of phase space distributions of stormtime proton ring current, *J. Geophys. Res.*, *99*, 5745-5759, 1994.

Davidson, G. T., An improved empirical description of the bounce motion of trapped particles, *J. Geophys. Res.*, *81*, 4029-4030, 1976.

Ejiri, M., Trajectory traces of charged particles in the magnetosphere, *J. Geophys. Res.*, *83*, 4798-4810, 1978.

Ejiri, M., A. A. Hoffman, and P. H. Smith, Energetic particle penetrations into the inner magnetosphere, *J. Geophys. Res.*, *85*, 653-663, 1980.

Fok, M.-C., J. U. Kozyra, A. F. Nagy, and T. E. Cravens, Lifetime of ring current particles due to Coulomb collisions in the plasmasphere, *J. Geophys. Res.*, *96*, 7861-7867, 1991.

Fok, M.-C., J. U. Kozyra, A. F. Nagy, C. E. Rasmussen, and G. V. Khazanov, Decay of equatorial ring current ions and associated aeronomical consequences, *J. Geophys. Res.*, *98*, 19,381-19,393, 1993.

Gloeckler, G., et al., The Charge-Energy-Mass (CHEM) spectrometer for 0.3 to 300 keV/e ions on AMPTE-CCE, *IEEE Trans. Geosci. Remote Sens.*, *GE-23*, 234-240, 1985.

Gonzalez, W. D., J. A. Joselyn, Y. Kamide, H. W. Kroehl, G. Rostoker, B. T. Tsurutani, and V. M. Vasyliunas, What is a geomagnetic storm? *J. Geophys. Res.*, *99*, 5771-5792, 1994.

Hamilton, D. C., G. Gloeckler, F. M. Ipavich, W. Stüdemann, B. Wilken, and G. Kremser, Ring current development during the great geomagnetic storm of February 86, *J. Geophys. Res.*, *93*, 14,343-14,355, 1988.

Harel, M., R. A. Wolf, P. H. Reiff, R. W. Spiro, W. J. Burke, F. J. Rich, and M. Smiddy, Quantitative simulation of a magnetospheric substorm 1. Model logic and overview, *J. Geophys. Res.*, *86*, 2217-2241, 1981.

Kistler, L. M., F. M. Ipavich, D. C. Hamilton, G. Gloeckler, B. Wilken, G. Kremser, and W. Stüdemann, Energy spectra of the major ion species in the ring current during geomagnetic storms, *J. Geophys. Res.*, *94*, 3579-3599, 1989.

Kivelson, M. G., S. M. Kaye, and D. J. Southwood, The physics of plasma injection events, *Dynamics of the Magnetosphere*, edited by S.-I. Akasofu, pp. 385-405, D. Reidel, Norwell, Mass., 1980.

Kozyra, J. U., C. E. Rasmussen, and L. R. Lyons, The interaction of ring current and radiation belt protons with ducted plasmaspheric hiss, 1, Diffusion coefficients and time scales, *J. Geophys. Res.*, *99*, 4069-4084, 1994a.

Kozyra, J. U., R. H. Miller, M.-C. Fok, B. J. Anderson, E. R. Sanchez, D. C. Hamilton, G. C. Ho, and D. S. Evans, A search for the scattering mechanism responsible for intense subauroral ion precipitation during the 7-10 February 1986 great magnetic storm, *Eos Trans. AGU*, *75*(16), Spring Meeting suppl., 304, 1994b.

LaBelle, J., and R. A. Treumann, Current-driven lower hybrid waves at the inner edge of the ring current, *J. Geophys. Res.*, *93*, 2591-2598, 1988.

Lennartsson, W., R. D. Sharp, E. G. Shelley, R. G. Johnson, and H. Balsiger, Ion composition and energy distribution during 10 magnetic storms, *J. Geophys. Res.*, *86*, 4628-4638, 1981.

Li, X., M. Hudson, A. Chan, and I. Roth, Loss of ring current O+ ions due to interaction with Pc 5 waves, *J. Geophys. Res.*, *98*, 215-231, 1993.

McIlwain, C. E., Magnetic coordinates, *Space Sci. Rev.*, *5*, 585-598, 1966.

McIlwain, C. E., Plasma Convection in the vicinity of the geosynchronous orbit, in *Earth's Magnetospheric Processes*, edited by B. M. McCormac, pp. 268-279, D. Reidel, Norwell, Mass., 1972.

Phaneuf, R. A., R. K. Janev, and M. S. Pindzola, Atomic data for fusion, vol. V, Collisions of carbon and oxygen ions with electrons, H, $H_2$ and He, *Tech. Rep. ORNL-6090/V5*, Oak Ridge Nat. Lab., Oak Ridge, Tenn., 1987.

Rairden, R. L., L. A. Frank, and J. D. Craven, Geocoronal imaging with Dynamics Explorer, *J. Geophys. Res.*, *91*, 13,613-13,630, 1986.

Rasmussen, C. E., S. M. Guiter, and S. G. Thomas, Two-dimensional model of the plasmasphere: Refilling time constants, *Planet. Space Sci.*, *41*, 35-43, 1993.

Roederer, J. G., *Dynamics of Geomagnetically Trapped Radiation*, Springer-Verlag, New York, 1970.

Roelof, E. C., Energetic neutral atom image of a storm-time ring current, *Geophys. Res. Lett.*, *14*, 652-655, 1987.

Roelof, E. C., and D. J. Williams, The terrestrial ring current: From in situ measurements to global images using energetic neutral atoms, *Johns Hopkins APL Tech. Dig.*, *9*, 144-163, 1988.

Roelof, E. C. and D. J. Williams, Update on global imaging using energetic neutral atoms, *Johns Hopkins APL Tech. Dig.*, *11*, 72-76, 1990.

Roelof, E. C., B. H. Mauk, and R. R. Meier, Instrument requirements for imaging the magnetosphere in extreme-ultraviolet and energetic neutral atoms derived from computer-simulated images, *Proc. SPIE Photo Opt. Instrum. Magnetospheric Imagery*, *1744*, 19-30, 1992.

Roth, I., B. I. Cohen, and M. K. Hudson, Lower hybrid drift instability at the inner edge of the ring current, *J. Geophys. Res.*, *95*, 2325-2332, 1990.

Rycroft, M. J., Some aspects of geomagnetically conjugate phenomena, *Ann. Geophys.*, *5A*, (6), 463-478, 1987.

Schulz, M., and L. J. Lanzerotti, Physics and Chemistry in Space, vol. 7, *Particle Diffusion in the Radiation Belts*, Springer, New York, 1974.

Sheldon, R. B., Ion transport and loss in the Earth's quiet ring current, 2, Diffusion and magnetosphere-ionosphere coupling, *J. Geophys. Res.*, *99*, 5705-5720, 1994.

Stern, D. P., The motion of a proton in the equatorial magnetosphere, *J. Geophys. Res.*, *80*, 595-599, 1975.

Stüdemann, W., et al., The May 2-3, 1986 magnetic storm: First energetic ion composition observations with the MICS instrument on Viking, *Geophys. Res. Lett.*, *14*, 455-458, 1987.

Volland, H., A semiempirical model of large-scale magnetospheric electric fields, *J. Geophys. Res.*, *78*, 171-180, 1973.

Williams, D. J., and M. Sugiura, The AMPTE Charge Composition Explorer and the 4-7 September 1984 geomagnetic storm, *Geophys. Res. Lett.*, *12*, 305-308, 1985.

Williams, D. J., E. C. Roelof, and D. G. Mitchell, Global magnetospheric imaging, *Rev. Geophys.*, *30*, 183-208, 1992.

Yeh, H.-C., and J. C. Foster, Storm time heavy ion flow at mid-latitude, *J. Geophys. Res.*, *95*, 7881-7891, 1990.

M.-C. Fok and T. E. Moore, ES83, Space Sciences Laboratory, NASA Marshall Space Flight Center, Huntsville, AL 35812.

D. C. Hamilton and G. C. Ho, Department of Physics, University of Maryland, College Park, MD 20742.

J. U. Kozyra, Space Physics Research Laboratory, Department of Atmospheric, Oceanic and Space Sciences, University of Michigan, Ann Arbor, MI 48109.